Efficient photocatalytic CO_2 reduction mediated by transitional metal borides: metal site dependent activity and selectivity

Li Shi [a#], Pei Wang [b#], Qi Wang [a,c], Xiaohui Ren [a,c], Fumihiko Ichihara [a,c], Wei Zhou [e], Hongwei Zhang [f], Yasuo Izumi [f], Ben Cao [b], Shengyao Wang [a,b], Hao Chen [b*], Jinhua Ye [a,c,d *]

[a] International Center for Materials Nanoarchitectonics (WPI-MANA), National Institute for Materials Science (NIMS), 1-1 Namiki, Tsukuba, Ibaraki, 305-0044, Japan.

[b] College of Science, Huazhong Agricultural University, Wuhan, 430070, P. R. China.

[c] Graduate School of Chemical Sciences and Engineering, Hokkaido University, Sapporo, 060-0814, Japan.

[d] TU-NIMS Joint Research Center, School of Materials Science and Engineering, Tianjin University, 92 Weijin Road, Nankai District, Tianjin 300072, P. R. China.

[e] Department of Applied Physics, Tianjin Key Laboratory of Low Dimensional Materials Physics and Preparing Technology, Faculty of Science, Tianjin University, Tianjin 300072, P. R. China.

[f] Department of Chemistry, Graduate School of Science, Chiba University, Yayoi 1-33, Inage-ku, Chiba 263-8522, Japan.

[#] These authors contributed equally to this work.

E-mail: Jinhua.YE@nims.go.jp; hchenhao@mail.hzau.edu.cn

Computational details

Spin-polarized and a standard dipole correction calculations were conducted with the Vienna Ab-initio Simulation Package (VASP 5.4.4)[1],[2]. The electron exchange and correlation were depicted with the generalized gradient approximation (GGA) utilizing Perdew–Burke–Ernzerhof (PBE) functional[3]. The electron-ion interaction was depicted by the projector augmented-wave formalism (PAW)[4],[5]. The plane wave cut-off energy is 400 eV, and the electronic self-consistent convergence is 10^{-6} eV. Geometries were converged to a residual force smaller than 0.02 eV/Å. The dipole correction was applied in the Z direction. The Brillouin zone was integrated by a $9 \times 9 \times 9$ and $5 \times 5 \times 1$ Monkhorst–Pack grid for bulk and slab models, respectively. The CO_2, CO and H_2 gas molecular, and liquid H_2O were calculated based on the previous work[6].

The optimized bulk Ni_3B, Co_3B, and Fe_2B lattice parameters were in good agreement with the experimental value as shown in Table S2[7-9]. The $Ni_3B(010)$, $Co_3B(010)$, and $Fe_2B(010)$ surface are modeled by a $\sqrt{3} \times \sqrt{3}$ supercell, and 9 layers with a total 48, 48, and 36 atoms respectively. The vacuum thickness was set at 15 Å to neglect the interaction between the adjacent slabs. The bottom 6 layers were fixed in its bulk position, while the top 3 layers were relaxed in the calculations. The $Ni_3B(010)$ surface could be terminated either by Ni or NiB layer, and its model was set by a periodic slab with several trilayers achieved from the bulk Ni_3B structure, and each trilayer was composed of three atomic monolayers, namely NiB-Ni-Ni. The case is the same for Co_3B, while for Fe_2B, the trilayer consists of B-Fe-Fe monolayers. Therefore, there were three kinds of (010) surfaces, namely as M-M-MB, M-MB-M, MB-M-M. The MB-M-M (B-M-M for Fe_2B) was chosen to represent (010) surface, due to it has the lowest surface energy and similar structures for the $Ni_3B(010)$, $Co_3B(010)$ and $Fe_2B(010)$ surfaces, as shown in FigureS6. And the structure of intermediate along the reaction path was shown in Figure S7.

The surface energy γ is described as,
$$\gamma = \frac{[(E_{slab} - NE_{bulk}) - \frac{1}{2}(E_{slab}^{unrel} - NE_{bulk})]}{A}$$
, where E_{slab}, E_{slab}^{unrel} and E_{bulk} stand for the total energies of the free relaxed upper three layers, the unrelaxed surface, and the

optimized unit cell bulk, respectively. A refers to the surface area, and N is the number of bulk units on the surface.

The free energy was obtained from the equation $G = E_{ele} + E_{vib} + E_t + E_r - TS$ as using the vaspkit (1.00 version) tool[10], where E_{ele}, E_t, E_r, and E_{vib} are the electronic, translational, rotational and vibrational energies, respectively. And S is the entropy, T was set to room temperature (298.15 K). where the frequency below 50 cm^{-1} was set to 50 cm^{-1}.

The computational hydrogen electrode (CHE, $H^+ + e^- \rightarrow 1/2\ H_2$, PH = 0) model has been used for the free energy of adsorbates[11], which involves proton-electron transfers as $\Delta G(U) = \Delta G_0 + neU$, where n refers to the transferred number of protons-electrons, and U stands for the potential versus the reversible hydrogen electrode (RHE), ΔG_0 is the free energy at U=0. The reaction barrier was also the limiting potential (U_L) is calculated by: $U_L = -\Delta G_0/e$.

The optimized bulk Ni lattice parameters is 3.521 Å, and it is consistent with the experimental value (3.524 Å). The Ni(111) surface is modeled by a $\sqrt{3} \times \sqrt{3}$ supercell, and 5 layers with a total of 45 atoms, with 15 Å vacuum thickness. The bottom 2 layers were fixed in its bulk position, while the top 3 layers were relaxed in the calculations. The Brillouin zone was integrated by an $11 \times 11 \times 11$ and $5 \times 5 \times 1$ Monkhorst–Pack grid for bulk and slab models, respectively. The adsorption energy of CO was calculated by reference to CO_2, H_2, and H_2O molecular, which is $\Delta G = G_{co/surf} - G_{surf} - G_{CO2} - G_{H2} + G_{H2O}$. Here $G_{co/surf}$, G_{surf}, G_{CO2}, G_{H2}, and G_{H2O} represents the free energies of CO adsorbed system, surface, CO_2 molecular, H_2 molecular, and liquid H_2O molecular, respectively. This was also the same energy of $\Delta G(CO^* + H2O(l))$ in reaction path.

The optimized bulk NiO lattice parameters of 4.180 Å were in good agreement with the experimental value (4.168 Å). Since GGA was not able to correctly describe the electronic structure of Ni^{4+}, we adopted the GGA+U approximation with the Dudarev ''+U'' term with a U-J value of 8.0 eV for the d electrons of Ni atoms[12].
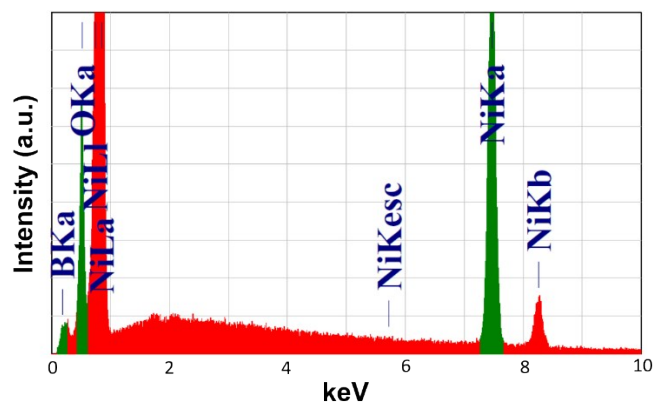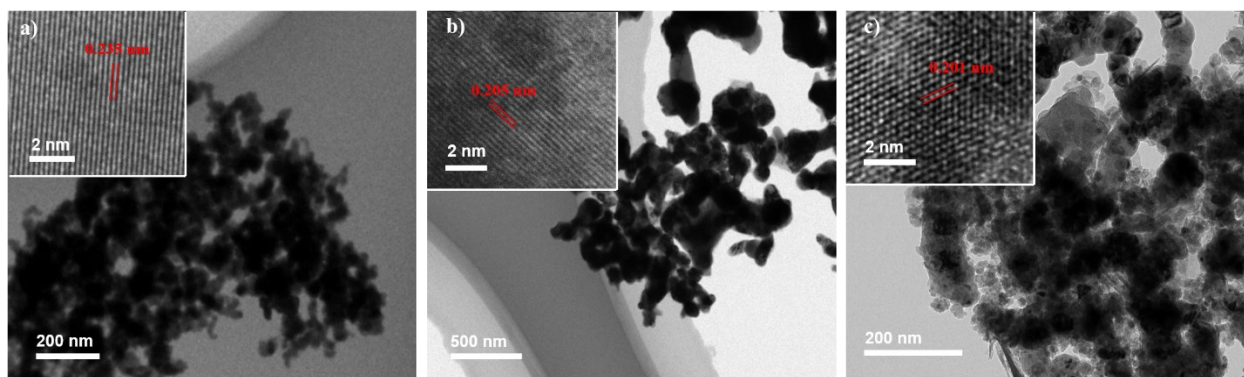
Figure S1. EDX spectrum of Ni_3B.

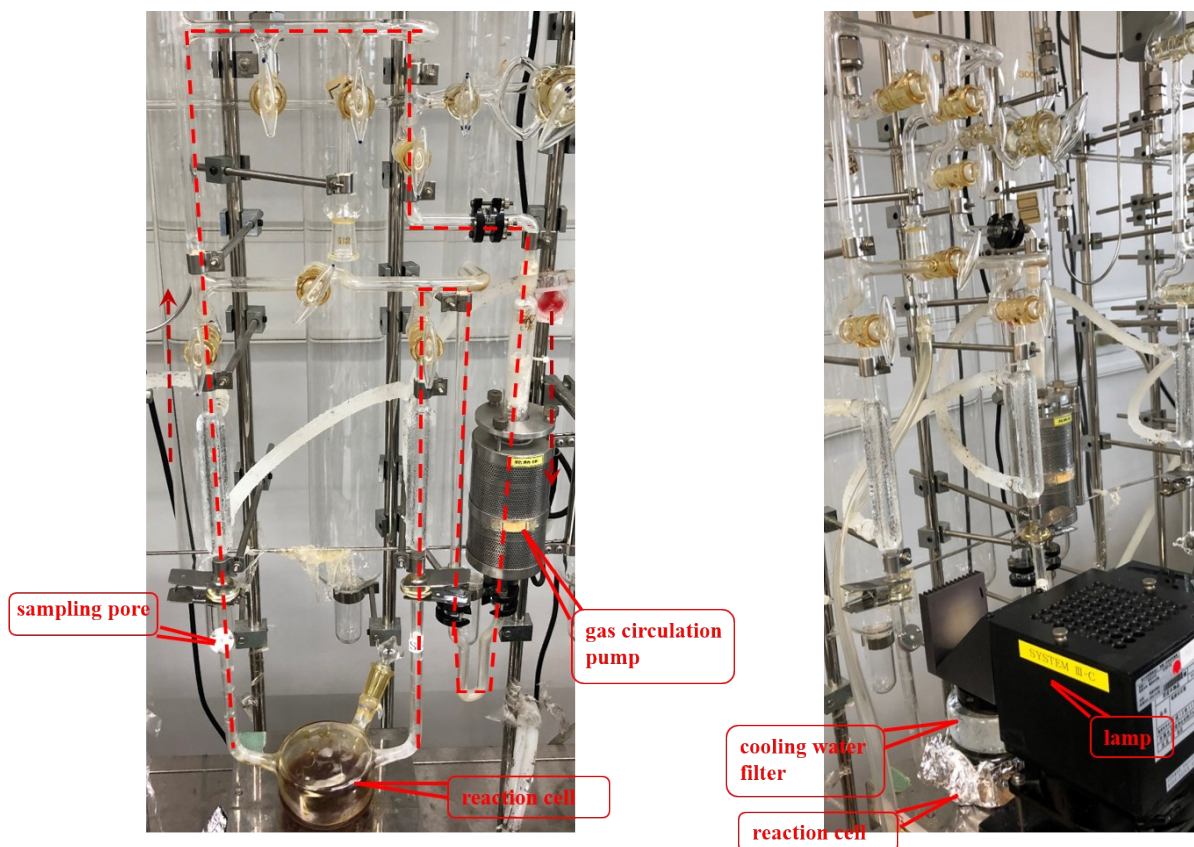Figure S2. TEM and HRTEM images of (a) Ni_3B, (b) Co_3B and (c) Fe_2B.

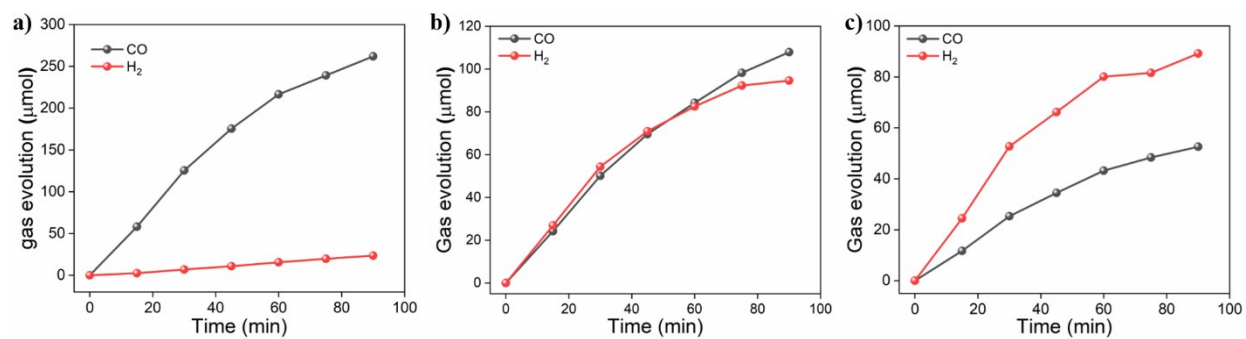Figure S3. Experimental setup of liquid-solid reaction mode for photocatalytic CO_2 reduction.

Figure S4. Time-dependent CO and H_2 evolution over (a) $Ni_3B/[Ru]$, (b) $Co_3B/[Ru]$ and (c) $Fe_2B/[Ru]$.

Table S1. Comparison of photocatalytic CO_2 activities over different cocatalysts in the [Ru] photosensitized systems.

| Cocatalysts	Photosensitizer/ sacrificial agent	Major product evolution rate (μmol h^{-1})	Selectivity	AQY	References
Ni$_3$B	[Ru]/TEOA	CO: 157.7	93.0%	4.5% at 420 nm	This work
N-doped carbon@NiCo$_2$O$_4$	[Ru]/TEOA	CO: 26.2	88.6%	1.07% at 420 nm	Energy Environ. Sci., 2018, 11, 306-310.
single-atom Co on graphene	[Ru]/TEOA	CO: 77.9	79.4%	/	Adv. Mater., 2018, 30, 1704624.
Nickel Metal–Organic Framework Monolayers	[Ru]/TEOA	CO: 12.5	97.8%	2.2% at 420 nm	Angew. Chem. Int. Ed., 2018, 57, 16811-16815.
Cobalt Imidazolate Metal–Organic Frameworks	[Ru]/TEOA	CO: 83.6	58.3%	1.48% at 420 nm	Angew. Chem. Int. Ed., 2014, 53, 1034-1038.
Co$_3$O$_4$ Hexagonal Platelets	[Ru]/TEOA	CO: 35.2	77.1%	0.069% at 450 nm	Adv. Mater., 2016, 28, 6485-6490.
Co-ZIF-67	[Ru]/TEOA	CO: 29.6	66.6%	1.55% at 420 nm	Appl. Catal. B: Environ, 2017, 209, 476-482.
CoSn(OH)$_6$	[Ru]/TEOA	CO: 19.3	86.46%	1.16% at 450 nm	ACS Sustainable Chem. Eng., 2017, 6, 781-786.
MnCo$_2$O$_4$	[Ru]/TEOA	CO: 27.0	77.1%	/	ACS Appl. Mater. Interfaces, 2015, 7, 4327-4335.
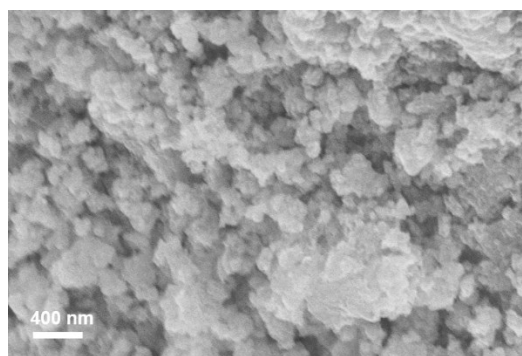
Figure S5. SEM image of Ni$_3$B after photocatalytic CO_2 reduction reaction.
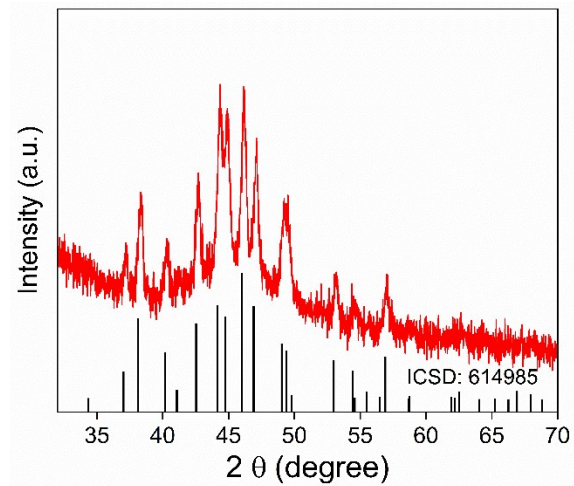
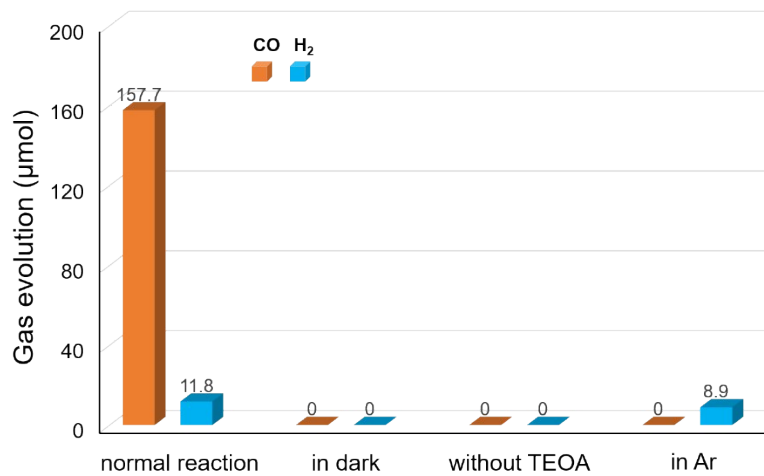Figure S6. XRD pattern of Ni_3B after photocatalytic CO_2 reduction reaction.

Figure S7. Production of CO and H_2 from the photocatalytic CO_2 reduction over Ni_3B/[Ru] under various reaction conditions. The reaction time is 1 hour.
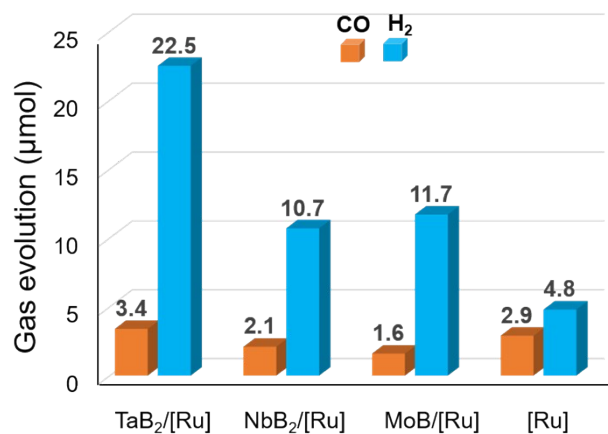
Figure S8. Production of CO and H_2 from the photocatalytic CO_2 reduction over TaB_2, NbB_2 and MoB cocatalysts in the presence of [Ru].

Table S2. The calculated lattice parameters (Experimental results are in parenthesis, Unit Å) of Fe_2B, Co_3B and Ni_3B, with lattice constants $\alpha = \beta = \gamma = 90°$.

Bulk	Experiment			optimization		
	a	b	c	a	b	c
Fe_2B	5.120	5.120	4.259	5.050	5.050	4.233
Co_3B	5.221	6.631	4.408	5.145	6.609	4.396
Ni_3B	5.211	6.619	4.389	5.197	6.629	4.390
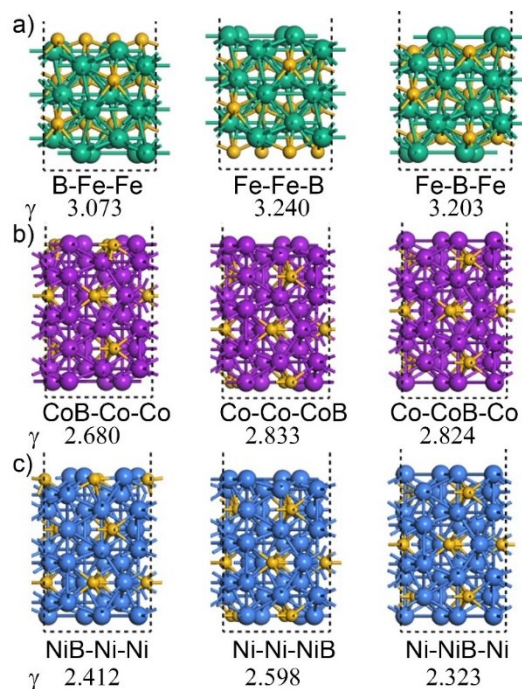
Figure S9. The three types and the corresponding surface energies γ (Unit: J/m^2) of (a) Fe$_2$B(010), (b) Co$_3$B(010), and (c) Ni$_3$B(010) surface. The green, purple, blue, and gold ball represents the Fe, Co, Ni, and B atom, respectively.
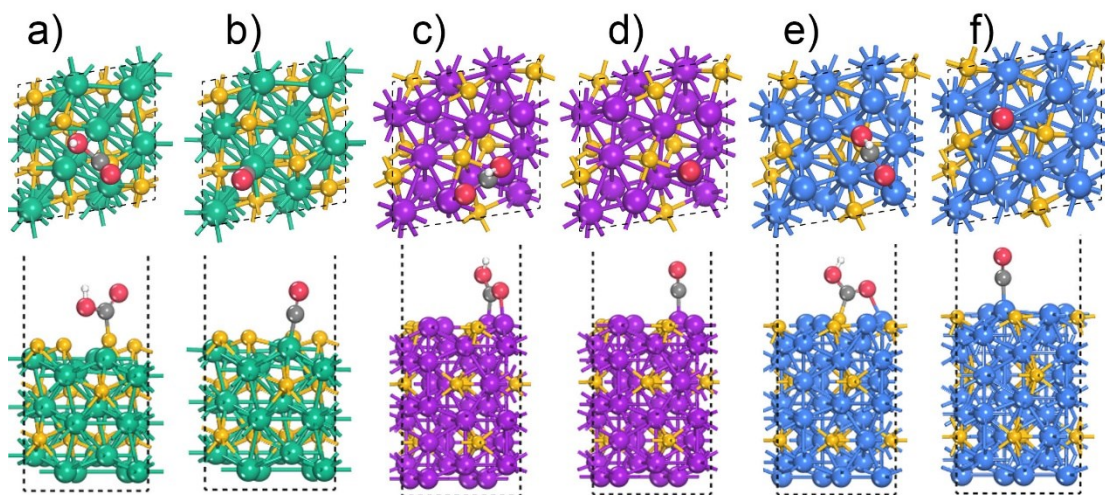

Figure S10. The intermediates of COOH and CO adsorbed on (a, b) Fe$_2$B(010), (c, d) Co$_3$B(010), and (e, f) Ni$_3$B(010) surface. The green, purple, blue, gold, red, grey, and white ball represents the Fe, Co, Ni, B, O, C, and H atom, respectively.
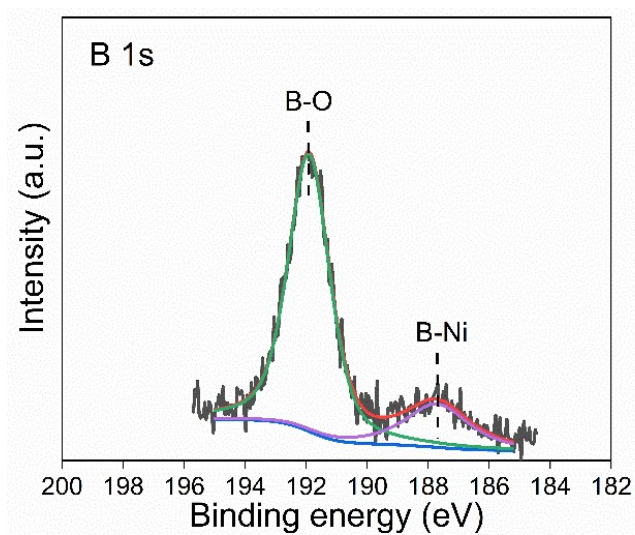
Figure S11. B 1s XPS spectrum of Ni$_3$B.
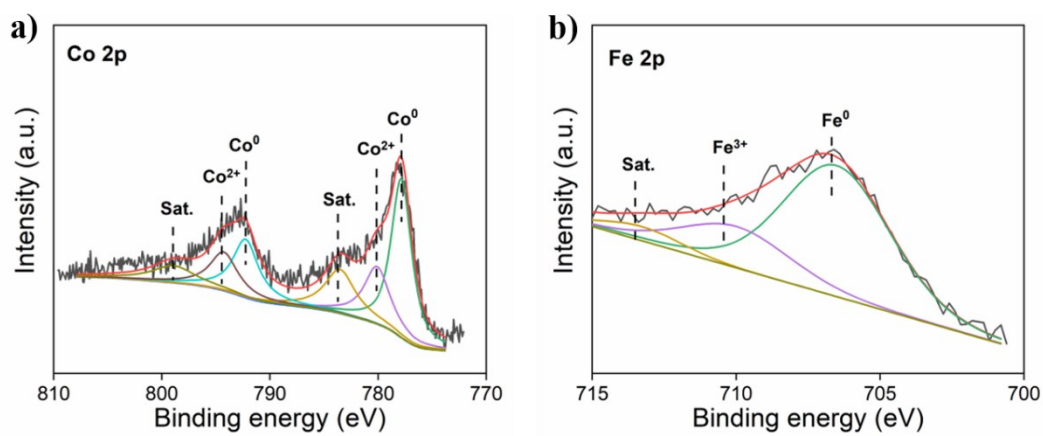
Figure S12. XPS spectra of (a) Co$_3$B and (b) Fe$_2$B.

Table S3. Fitted data of the time-resolved PL decay spectra.

Sample	A1	T1	A2	T2	Average lifetime
[Ru]	2889.65142	0.38393	2916.48524	0.38394	0.38394
Ni_3B/[Ru]	3766.4592	0.03645	6711.81536	0.50584	0.48760
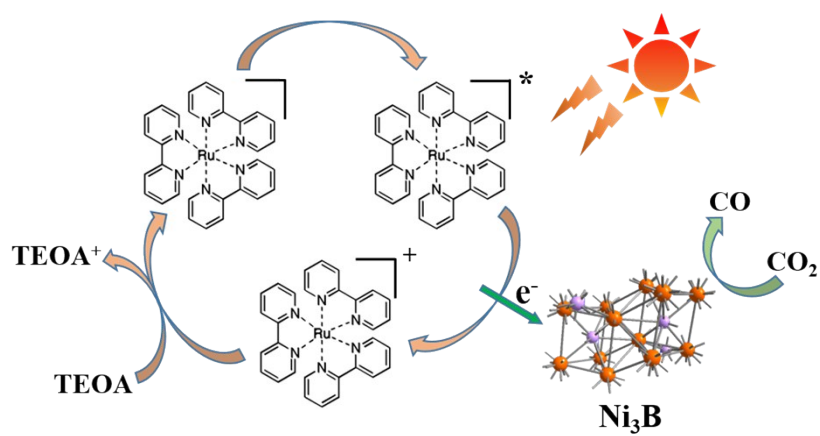
Figure S13. Proposed mechanism for the photocatalytic reduction of CO_2 to CO over [Ru] photosensitized Ni_3B visible light irradiation
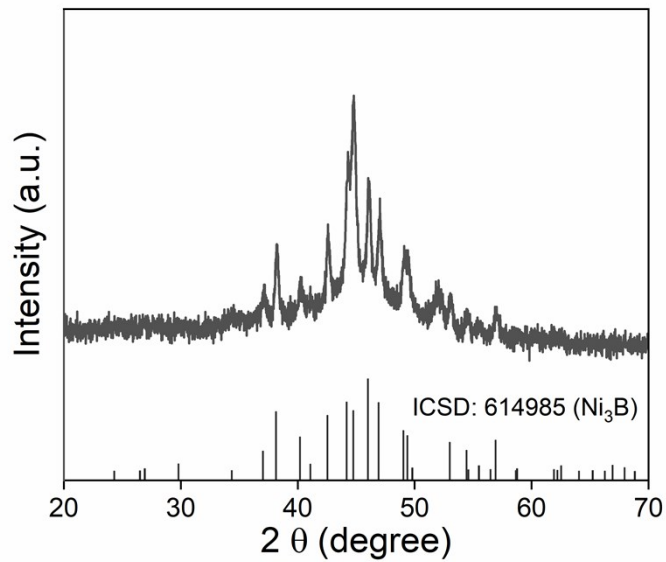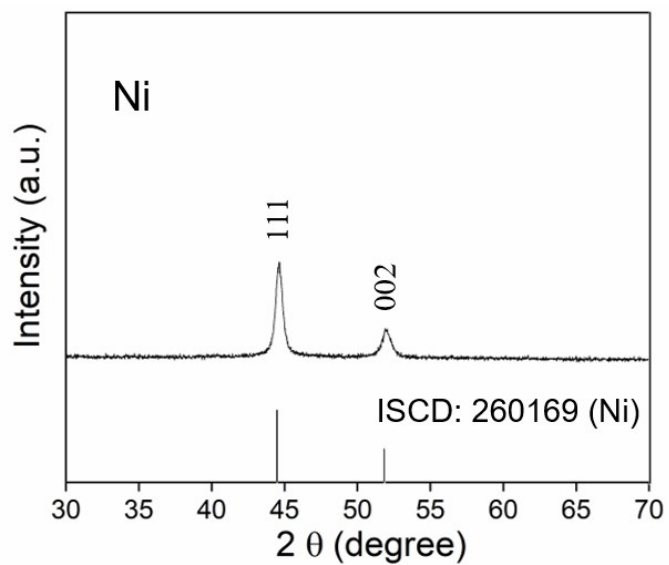
Figure S14. XRD patterns of air treated Ni$_3$B.

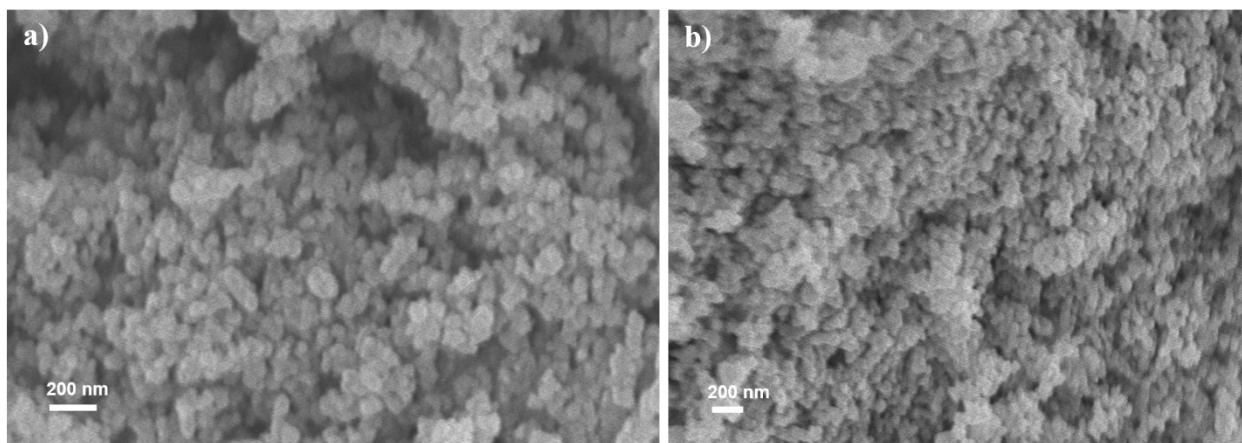Figure S15. XRD patterns of H$_2$ treated Ni$_3$B.

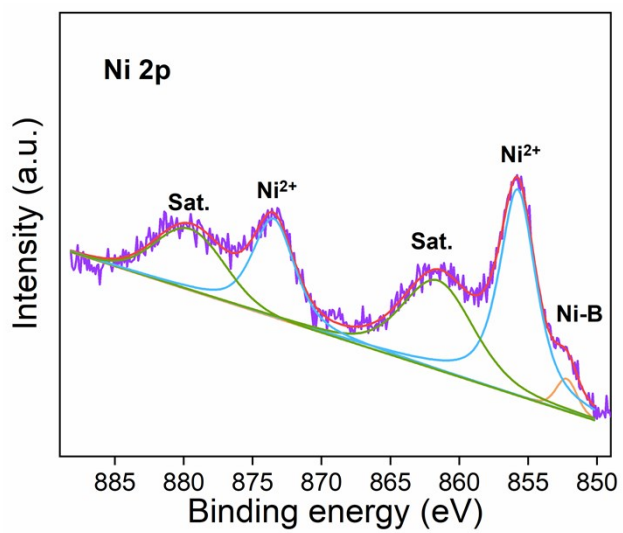Figure S16. SEM images of (a) air treated Ni_3B and (b) H_2 treated Ni_3B.
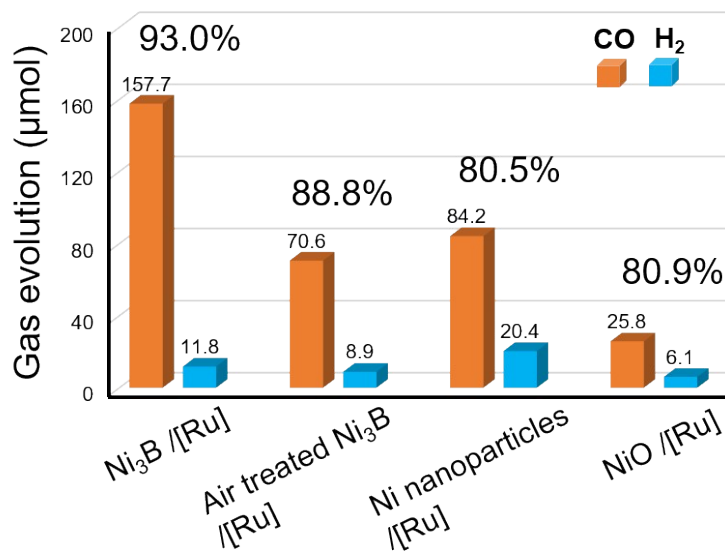

Figure S17. XPS spectra of air treated Ni_3B.

Figure S18. Photocatalytic CO_2 reduction performances of Ni_3B, air treated Ni_3B, Ni nanoparticles and NiO in the presence of [Ru]. The reactions are conducted for 1 hour. NiO was commercially obtained from Sigma-Aldrich.
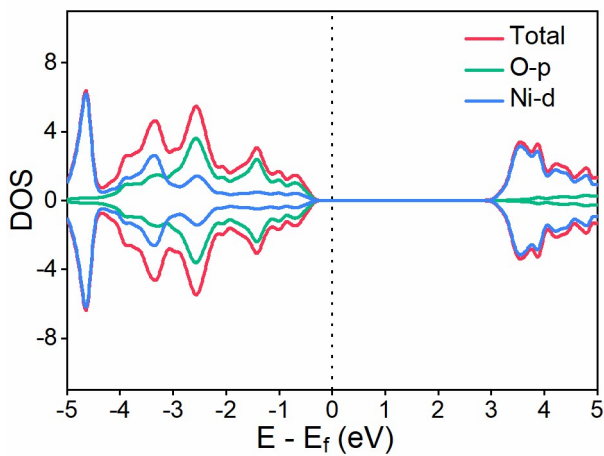

Figure S19. Calculated DOS of NiO. The DOS shows obvious bandgap in the NiO, indicating its semiconducting feature.
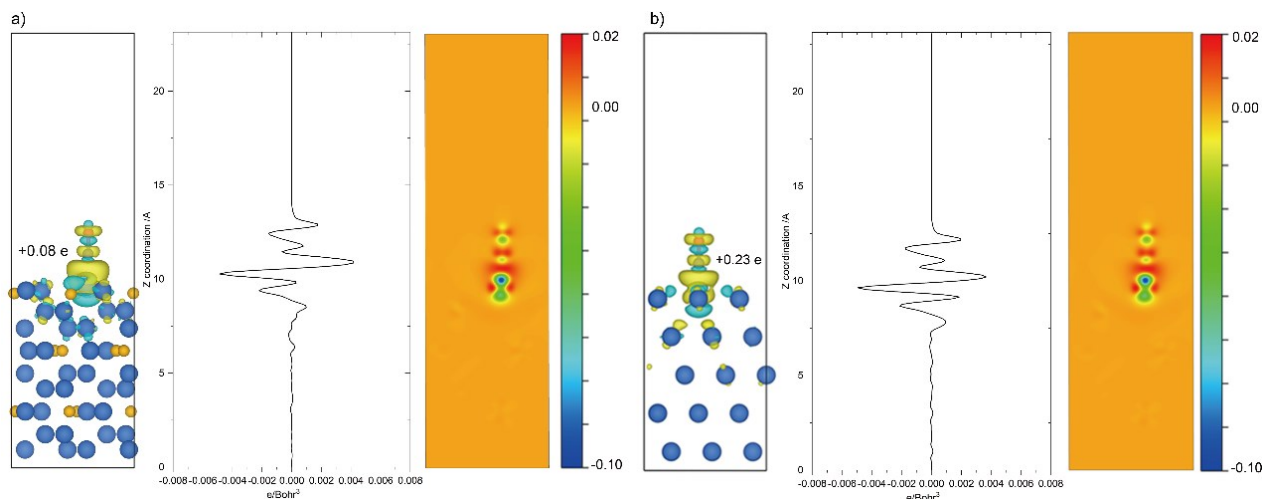
Figure S20. Charge density difference with 3D (left) and 2D (right) plot, and planar average differential charge density on the z-axis (middle) of (a) $CO/Ni_3B(010)$ system and (b) $CO/Ni(111)$ system, with isosurfaces value of $0.002e/Bohr^3$, which CO is adsorbed on the top site. The cyan and yellow color corresponds to accumulation and depletion of charge, respectively. The corresponding charge transfer from surface to CO was marked from Bader charge analysis. The blue, gold red, and grey ball represents the Ni, B, O, and C atom, respectively.

References

[1] G. Kresse, J. Hafner, *Phys. Rev. B* **1993**, 47, 558-561.

[2] G. Kresse, J. Furthmüller, *Phys. Rev. B* **1996**, *54*, 11169-11186.

[3] J. P. Perdew, K. Burke, M. Ernzerhof, *Phys. Rev. Lett.* **1996**, *77*, 3865-3868.

[4] P. E. Blöchl, *Phys. Rev. B* **1994**, *50*, 17953-17979.

[5] G. Kresse, D. Joubert, *Phys. Rev. B* **1999**, *59*, 1758-1775.

[6] P. Wang, S. N. Steinmann, G. Fu, C. Michel, P. Sautet, *ACS Catal.* **2017,** *7*, 1955-1959.

[7] C. Kapfenberger, B. Albert, R. Pöttgen, H. Huppertz, *Crystalline Materials*, **2006**, *221*, 477-481.

[8] R. M. A. Fruchart, *BULLETIN DE LA SOCIETE CHIMIQUE DE FRANCE* **1959,** *2*, 422-423

[9] S. Rundqvist, *Nature* **1958,** *181*, 259-260.

[10] V. Wang, N. Xu, VASPKIT: A pre-and post-processing program for the VASP code, 2013[J].

[11] A. A. Peterson, F. Abild-Pedersen, F. Studt, J. Rossmeisl, J. K. Nørskov, *Energ. Environ. Sci.* **2010,** *3*, 1311-1315.

[12] V. I. Anisimov, J. Zaanen, O. K. Andersen, *Phys. Rev. B* **1991,** 44, 943-954.